OAK RIDGE
NATIONAL LABORATORY
MANAGED BY UT-BATTELLE
FOR THE DEPARTMENT OF ENERGY

ORNL/TM-2013/84

Light Water Reactor Sustainability Program

Updates of high-fluence induced microstructural evolution of austenitic stainless steels under LWR relevant conditions

February 2013

Prepared by

L. Tan and J.T. Busby
Oak Ridge National Laboratory

UT-BATTELLE
ORNL-27 (4-00)

ORNL/TM-2013/84

Light Water Reactor Sustainability

Updates of high-fluence induced microstructural evolution of austenitic stainless steels under LWR relevant conditions

L. Tan and J.T. Busby
Oak Ridge National Laboratory

Date Published: February 2013

Prepared under the direction of the
U.S. Department of Energy
Office of Nuclear Energy
Light Water Reactor Sustainability
Materials Aging and Degradation Pathway

Prepared by
OAK RIDGE NATIONAL LABORATORY
Oak Ridge, Tennessee 37831-6283
managed by
UT-BATTELLE, LLC
for the
U.S. DEPARTMENT OF ENERGY
under contract DE-AC05-00OR22725

This page intentionally left blank

CONTENTS

Page

This page intentionally left blank

LIST OF FIGURES

Figure **Page**

This page intentionally left blank

LIST OF TABLES

Table **Page**

This page intentionally left blank

ACKNOWLEDGMENTS

This research was sponsored by the U.S. Department of Energy, Office of Nuclear Energy, for the Light Water Reactor Sustainability Research and Development effort.

This page intentionally left blank

EXECUTIVE SUMMARY

Components serving in a nuclear reactor plant must withstand a very harsh environment including extended time at temperature, neutron irradiation, stress, and/or corrosive media. The many modes of degradation are complex and vary depending on location and material. However, understanding and managing materials degradation is a key for the continued safe and reliable operation of nuclear power plants.

For the reactor core and primary systems, several key areas have been identified. Thermo-mechanical considerations such as aging and fatigue must be examined. Irradiation-induced processes must also be considered for higher fluences, particularly the influence of RIS, swelling, and/or precipitation on embrittlement. Corrosion takes many forms within the reactor core, although IASCC and PWSCC are of high interest in extended life scenarios. Research in these areas can build upon other ongoing programs in the LWR industry as well as other reactor materials programs (such as fusion and fast reactors) to help resolve these issues for extended LWR life.

Phase transformations are being observed for a variety of materials and operating conditions of austenitic steels in light water reactors that may impact component lifetime as plants strive towards longer lifetimes. This form of degradation may become visible in a number of components including core barrels, baffle plates, baffle bolts, top guides, and support plates. All of these components are made from austenitic stainless steels including 304, 316, and 347 grades. Of these grades, 316 may be the most susceptible to the formation of G and γ' phases due to the higher Ni content. 304 and 347 may be more likely to undergo martensitic transformations due to their lower austenite stability. More detailed analysis is required to bind the effects of this issue, and the purpose of this report is to update the recent analysis of irradiation-induced phase transformations in austenitic stainless steels. This update focuses on transmission electron microscopy (TEM) characterization. The results and implications are discussed below.

Samples KS13 (AISI 304 + Ni) and PS15 (AISI 304 + Mo + Hf), which were irradiated in BOR-60 at ~320°C for 9.6 dpa, have been characterized using TEM and related techniques. The Ni addition in the KS13 favored the coarsening or unfaulting of Franking loops, leading to reduced density and increased size. In contrast, the (Ni + Cr) addition in the previously characterized LS13 (AISI 304 + Ni + Cr) did not significantly alter the evolution of Frank loops, which followed the evolution trend of Frank loops in the AS13 (industrial 304 at 5.5 dpa) and AS18 (industrial 304 at 10.2 dpa). Frank loops characterization in the PS15 is in progress. A few tiny voids were observed in the KS13, which would generate slightly smaller swelling compared to the AS13 and AS18. This is approximately consistent with density measurements of the samples reported previously.

Large Cr-rich $M_{23}C_6$ (~0.2 μm) and Laves phase $(Fe,Ni)_2(Hf,Mo)$ (sub-micrometer to micrometer), pre-existing in the non-irradiated samples, were observed in the KS13 and PS15, respectively, which retained crystalline under the irradiation. The amount of $M_{23}C_6$ in the KS13 was less than that in the LS13, which is consistent with thermodynamic predictions. In addition to the pre-existing phases, some radiation-promoted phases in nanoscales were observed in the samples. They include cubic-on-cubic $M_{23}C_6$ particles (~50 nm) that was observed in the LS13 but not in the KS13, cubic-on-cubic G-phase or $M_{23}C_6$ particles (<~8 nm) with a density on the order of 10^{22} m^{-3} in both the KS13 and LS13, and a high density (10^{23} m^{-3}) of (Ti,Cr)N (~3 nm) in all the examined samples (except for HfC in the PS15). The identification of the ultrafine particles was based on their diffraction patterns and thermodynamic predictions of the alloys. Further investigation, primarily chemical analyses, is needed to confirm the phases of the ultrafine particles.

This page intentionally left blank

1. BACKGROUND

Nuclear power currently provides a significant fraction of the United States' non-carbon emitting power generation. In future years, nuclear power must continue to generate a significant portion of the nation's electricity to meet the growing electricity demand, clean energy goals, and ensure energy independence. New reactors will be an essential part of the expansion of nuclear power. However, given limits on new builds imposed by economics and industrial capacity, the extended service of the existing fleet will also be required.

Nuclear reactors present a very harsh environment for components service. Components within a reactor core must tolerate high temperature water, stress, vibration, and an intense neutron field. Degradation of materials in this environment can lead to reduced performance, and in some cases, sudden failure.

Irradiation-induced processes must be carefully considered for higher fluences, particularly the influence of RIS, swelling, and/or precipitation on embrittlement. The nominal irradiation temperature in LWRs is ~290°C; however, actual component temperatures range from 270°C to 370°C depending on the relative position of the component within the reactor core and relative amounts of cooling and gamma heating.

Extending the service life of a reactor will increase the total neutron fluence to each component. The neutron irradiation field can produce large property and dimensional changes in materials. This occurs primarily via one of five radiation damage processes: radiation-induced hardening and embrittlement, phase instabilities from radiation-induced or -enhanced segregation and precipitation, irradiation creep due to unbalanced absorption of interstitials vs. vacancies at dislocations, volumetric swelling from cavity formation, and high temperature helium embrittlement due to formation of helium-filled cavities on grain boundaries. For light water reactor systems, high temperature embrittlement and creep are not common problems due to the lower reactor temperature. However, radiation embrittlement, phase transformation, segregation, and swelling have all been observed in reactor components. The rest of this assessment will focus on irradiation-induced phase transformations.

Under irradiation, the large concentrations of radiation-induced defects will diffuse to defect sinks such as grain boundaries and free surfaces. These concentrations are in far excess of thermal-equilibrium values and can lead to coupled-diffusion with particular atoms. In engineering metals such as stainless steel, this results in radiation-induced segregation of elements within the steel. For example, in 316 stainless steel, chromium (important for corrosion resistance) can be depleted at areas while elements like nickel and silicon are enriched to levels well above the starting, homogenous composition. While radiation-induced segregation does not directly cause component failure, it can influence corrosion behavior in a water environment. Irradiation-induced changes of alloy microstructure may also lead to embrittlement and susceptibility to mechanical failure. Further, this form of degradation can accelerate the thermally-driven phase transformations mentioned above and also result in phase transformations that are not favorable under thermal aging (such as gamma or gamma-prime phases observed in stainless steels). Additional fluence may exacerbate radiation-induced phase transformations and should be considered.

A myriad of different phases have been observed including ferrite, several carbides, borides and phosphides, sigma, chi and Laves phases, as well as γ', G and η (eta) silicides. It should be noted that several of these phases ($M_{23}C_6$, M_6C, G and η silicides) have fcc structures with similar lattice spacings (1.06-1.1 nm, very close to three times that of the austenite matrix). As RIS may affect the

composition of both the precipitates and the surrounding matrix, precipitate lattice parameter measurement in the TEM may not be definitive alone for phase identification. Much of the data has been generated in fast reactor studies at higher temperatures where thermal kinetics and RIS are more pronounced.

In addition, irradiation-induced changes of alloy microstructure may lead to embrittlement. Long-term exposure of internal components will lead to high fluences and may result in irradiation-induced effects not yet observed in LWR conditions, although this form of degradation has been observed in fast reactor conditions. Under the LWRS Materials Aging and Degradation Pathway, a research task to provide detailed microstructural analysis of phase transformation in key samples and components (both model alloys and service materials), including transmission electron microscopy, magnetic measurements, and hardness examinations has been initiated. Mechanical testing to quantify any impacts on embrittlement may also be performed. These results will be used to develop and validate a phenomenological model of phase transformation under LWR conditions. The objective of this report is to detail recent testing and analysis results.

2. EXPERIMENTAL PROCEDURES AND MATERIALS

2.1. ALLOYS COMPOSITION AND STRUCTURE

The set of investigated alloys in this program includes industrial AISI 304 and 316 steels (marked as A, B, B1, C, and SW) and single-variable high purity austenitic model alloys (marked as E, H, G, I, K, L, M, and P). Composition of the alloy E was close to 304 steel, and the others 5 model alloys were the modifications of alloy E by additions of Si (alloy H), Mo (alloy G), P (alloy I), Mo+Hf (alloy P), Ni (alloy K), Ti, (alloy M) and Ni+Cr (alloy L). The element composition of the investigated alloys is given in Table 1.

Table 1. Damage dose, element composition (wt. %)*, pre-irradiation conditions, and grain size for investigated alloys

Alloy	Max.dose, dpa	Condition	C	**Mn**	**Si**	**Cr**	**Ni**	**Mo**	N	Grain size, mkm
A	47	Annealed	0.023	1.82	0.56	19.95	10.8	0.53	0.072	38
B	10.2	CW(ε~0.6)	0.056	1.13	0.73	16.84	10.54	2.25	0.021	47
B1	25	CW(ε~0.2)	0.056	1.13	0.73	16.84	10.54	2.25	0.021	29
C	4.8	CW(ε~0.4)	0.07	1.4	0.56	16.77	12.78	2.18	0.008	15
E	11.8	CW(ε~0.3)	0.021	0.94	0.04	18.76	12.37	0.04	0.0003	48
G	11.8	CW(ε~0.3)	0.02	0.97	0.03	18.26	12.15	2.36	0.0004	72
H	7.8	Annealed	0.02	1.01	1.05	18.17	12.45	0.02	0.0005	32
I	–	Annealed	0.02	1.01	1.05	18.17	12.45	0.02	0.0005	27
K	9.6	Annealed	0.02	1	0.03	18.21	25.08	0.02	0.0005	24
L	9.1	Annealed	0.02	1.02	0.03	25.22	25.07	0.02	0.0005	26
M	–	Annealed	0.02	1.00	0.03	18.03	11.22	0.02	0.0005	24
P	9.6	Annealed	0.028	1.01	0.1	17.03	13.6	2.18	n/d	19
SW	4.4	Annealed	0.022	1.07	0.24	18.42	10.45	n/d	0.025	67

* In all alloys: P<0.01%; S<0.01%; Ti < 0.02; Nb < 0.005. Alloy P contains also 1.17% Hf.

The alloys were produced for cooperative program of irradiation-assisted stress corrosion cracking research [1]. Material science aspects of alloys production and samples preparation are described in details in [2]. Alloys were irradiated in Russian BOR-60 fast reactor to damage dose 4.4 to 47 dpa at a damage dose rate of ~8×10^{-7} dpa×c-1 and 603 K (see Table 1). The irradiation temperature was close enough to the typical work temperature of industrial water reactors. The samples were irradiated in contact with coolant (sodium). More details are given in [3].

According to [2], all alloys were annealed prior to irradiation. However, during mechanical test of nonirradiated samples and post-radiation metallography examination, it was shown that alloys B, B1, C, E, and G were cold-worked prior irradiation (see Fig. 1). Degree of cold work (see Table 1) was estimated using mechanical test data reported in [3] and results of metallography research.

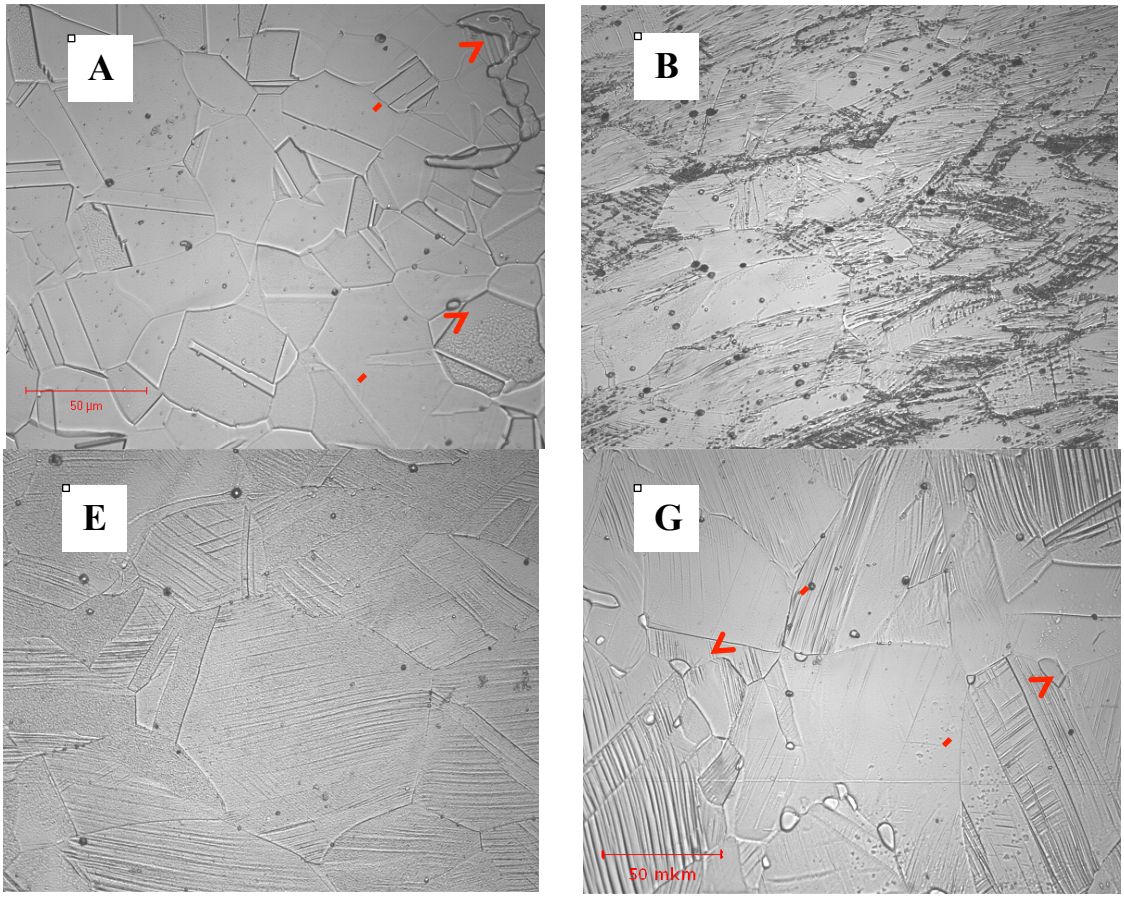

Fig.1. Typical metallographic structure of investigated irradiated alloys. Arrows show retained δ-ferrite in alloys A and G. Magnification is the same for all images. Etching by 10% oxalic acid at 6V during 80 sec. Alloys B, E, and G contain signs of pre-irradiation cold-work.

Irradiated samples for the present work were cut off from the ends of tensile dog bone specimens which geometry is described in details in [2]. The irradiated samples had dimensions 3.5 by 5 mm and thickness 1 to 1.2 mm. It was possible to expect that a modified surface layer exists on the samples due to contact with sodium coolant. For example, as shown in [4], for 16000 hours irradiation at 793K the thickness of carburized zone was found to be ~60 microns. In order to avoid any contamination caused effects, samples were polished mechanically, and layers of ~200 microns thickness were removed from both sides. The dimensions of nonirradiated samples varied from 3.5 by 4 mm to 10 by 10 mm with 1 mm thickness. Non-irradiated alloy SW and irradiated alloys M and I were not available. Non-irradiated samples of alloy A obtained from archive had a different grain size and most probably belonged to a different heat than the irradiated samples.

2.2. TRANSMISSION ELECTRON MICROSCOPY ANALYSIS

Material microstructures were characterized using transmission electron microscopy (TEM) techniques on a FEI CM200 field-emission-gun (FEG) TEM. Three-mm diameter discs were

sectioned from the tab section of tensile samples, ground down to <~150 μm thickness. Then, the samples were electropolished at -12°C in a methanol: sulfuric (7 : 1) solution using a Struers Tenupol polishing unit. A range of magnifications was used to record the microstructures at different sizes. The characterization included phase identification, grain boundary chemical analysis, and statistical quantitative analysis of the radiation-induced Frank loops and possible voids. Specimen thickness was estimated using convergent beam electron diffraction (CBED). Conventional TEM and scanning transmission electron microscopy (STEM) modes coupled with selected area diffraction (SAD) and energy dispersive X-ray spectroscopy (EDS) were used in this work to characterize morphology, identify phase and chemistry.

3. TRANSMISSION ELECTRON MICROSCOPY ANALYSIS

The samples of KS13 and PS15, irradiated at about 320°C for 9.6 dpa, were characterized using the similar TEM imaging techniques for the AS13, AS18, and LS13 samples that were reported previously [5]. Both the samples are based on an AISI 304 alloy. The KS13 and PS15 are alloyed with an additional (12.71% of Ni) and (2.14% Mo + 1.17% Hf), respectively, in weight percentages. The KS13 was annealed at 950°C for 30 min and the PS15 at 1100°C for 60 min.

3.1. KS13 (AISI304 + NI)

The electron diffraction pattern of the KS13 sample at the beam direction of [011] is shown in the left image of Fig. 2. As set of faint diffraction pattern is well aligned with the strong diffraction spots from the austenitic matrix. The 1/3 space relationship between the faint and strong spots suggests that the cubic-on-cubic precipitates in the matrix would be either $M_{23}C_6$ (Cr-rich) or G-phase (Ni/Si-rich). A two-beam condition, as shown in the right image of Figure 1, was obtained by tilting about 8° from the zone axis. Rel-rods are visible between (200) and (11-1) spots as well as a few faint "1/3" spots and faint ring patterns.

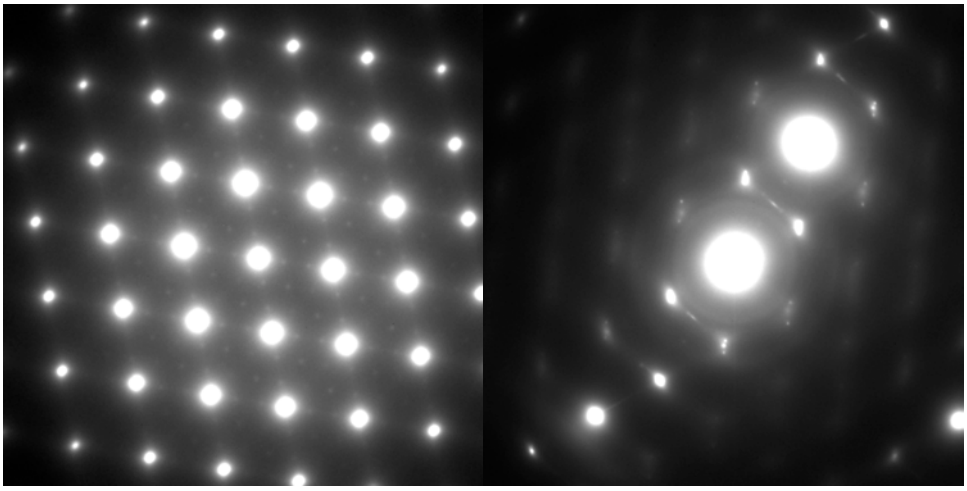

Fig. 2. Diffraction patterns at B=[011] (left) and a two-beam condition near [011] (right).

Figure 3 shows bright-field (BF) and dark-field (DF) images using the rel-rod in the right image of Fig. 2. Compared to the bright-field image, the radiation-induced Frank loops are clearly revealed under the dark-field. Statistical analysis of the Frank loops from multiple dark-field images led to an average size of 10.1±4.8 nm with a density of $(5.3\pm2.3)\times10^{22}$ m^{-3}. In addition to the Frank-loops, the dark-field image also reveals some ultrafine particles, which are originated from the "1/3" spot and ring adjacent to the rel-rod. The smallest size aperture could not individually encircle these diffraction features.

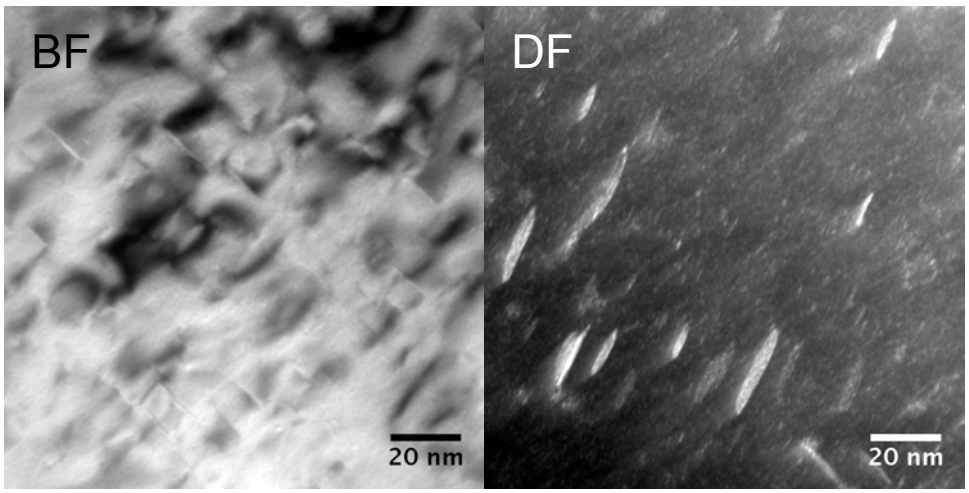

Fig. 3. Bright-field image and corresponding rel-rod dark-field image.

To have a better image of the ultrafine particles, careful adjustments had been conducted, which include the imaging location and the selected area primarily encircling the "1/3" spot for dark-field imaging. The bright-field image in Fig. 4 shows a high density of ultrafine particles with a size less than ~8 nm. Its dark-field image in Fig. 4 still shows a few Frank loops in addition to the many ultrafine particles. Reliable particle density could not be obtained because of the low contrast of the particles. According to the interspacing of the particles, the density of the ultrafine particles is estimated in the order of 10^{22} m^{-3}.

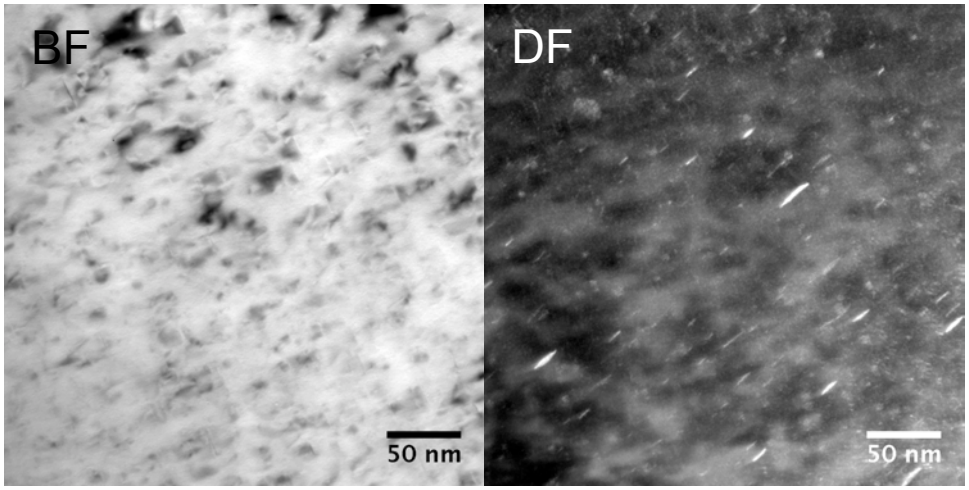

Fig. 4. Bright-field and dark-field images of the ultrafine particles.

By slightly tilting from the two-beam condition in Fig. 2, an intensified diffraction ring pattern was obtained as shown in Fig. 5. The dark-field image in Fig. 5 was taken using the diffraction ring(s) between the (-11-1) and (11-1) spots. No Frank loops (or rel-rod) were observed under this imaging condition. A high density of ultrafine particles is easily revealed in the dark-field image, which is

estimated in the order of 10^{23} m^{-3} with a size about 3 nm. According to the viewable rings in Fig. 5, they agree with a face-centered cubic structure with a lattice parameter of ~0.414 nm, which close to TiN/C or metastable CrN/C. Further analysis is needed to confirm this phase.

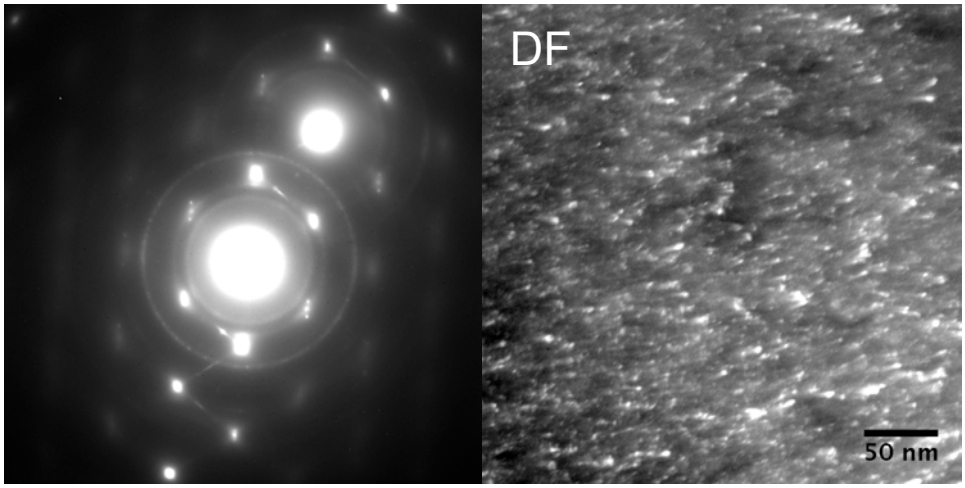

Fig. 5. Dark-field image of the diffraction rings.

Only a few Cr-rich carbides were observed in the KS13. Most of them are in a size of ~0.2 μm and primarily located at grain boundaries as shown in the left image of Fig. 6. The right image in Fig. 6 shows several ultrafine voids with a size less than 2 nm.

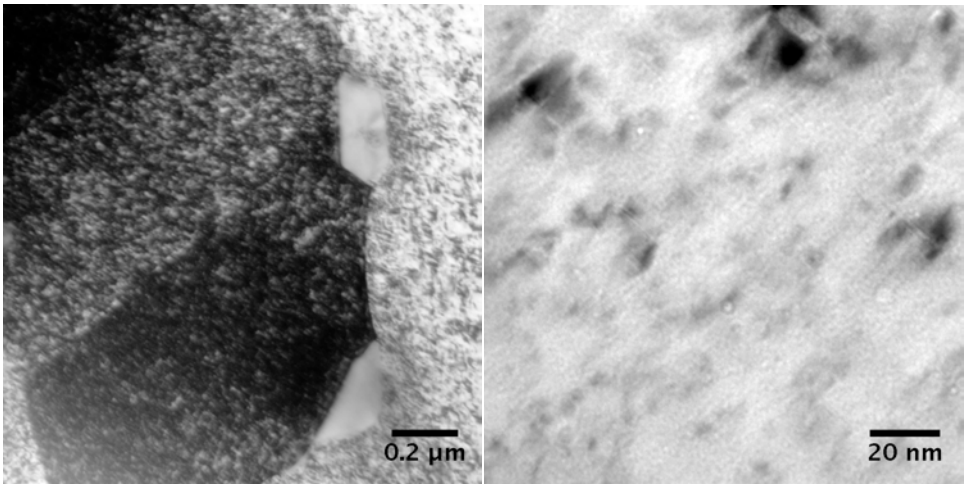

Fig. 6. Bright-field images revealing Cr-rich carbides (left) and a few ultrafine voids (right).

3.2. PS15 (AISI304 + MO + HF)

The PS15 sample has been preliminarily characterized. A near [011] two-beam condition was

acquired as shown in Fig. 7 to image Frank loops using the rel-rod. The dark-field image did not reveal distinctive Frank loops due to the slightly thicker sample. Further characterization by exploring better locations will be pursued.

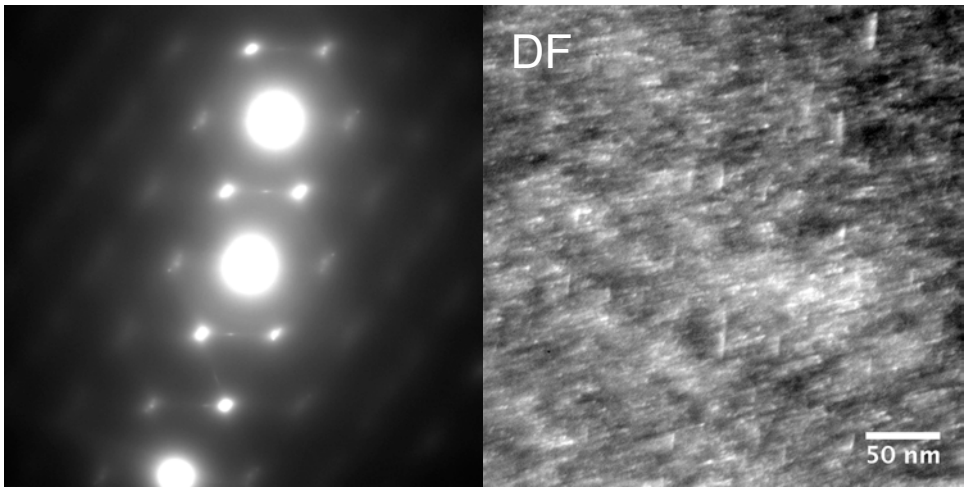

Fig. 7. Rel-rod imaging of the PS15 sample.

Many sub-micrometer size particles as shown in Fig. 8 were observed in the PS15, which exist inside grains or at grain boundaries. The right image in Fig. 8 shows an enlarged image of one of the particles. Energy dispersive X-ray spectroscopy analyses of the particles suggest that the particles may be $(Fe,Ni)_2(Hf,Mo)$ Laves phase.

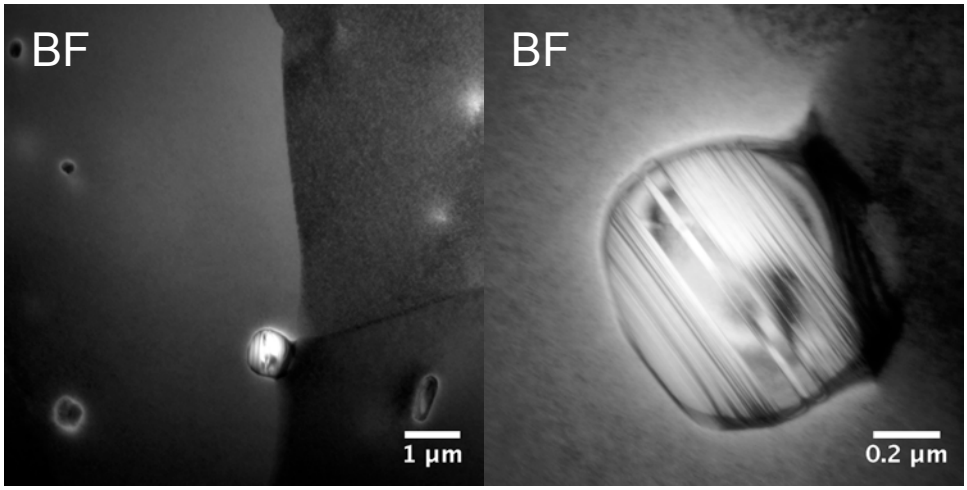

Fig. 8. Large particles in the PS15 sample.

Diffraction ring pattern was also observed in the PS15 sample, which is similar to that in the KS13 sample. Figure 9 shows the diffraction rings and the corresponding bright-field and dark-field

images. The ultrafine particles, resulting in the diffraction rings, had a density of 1.2×10^{23} m^{-3} with a size less than ~3 nm that are similar to those in Fig. 5 of KS13 sample.

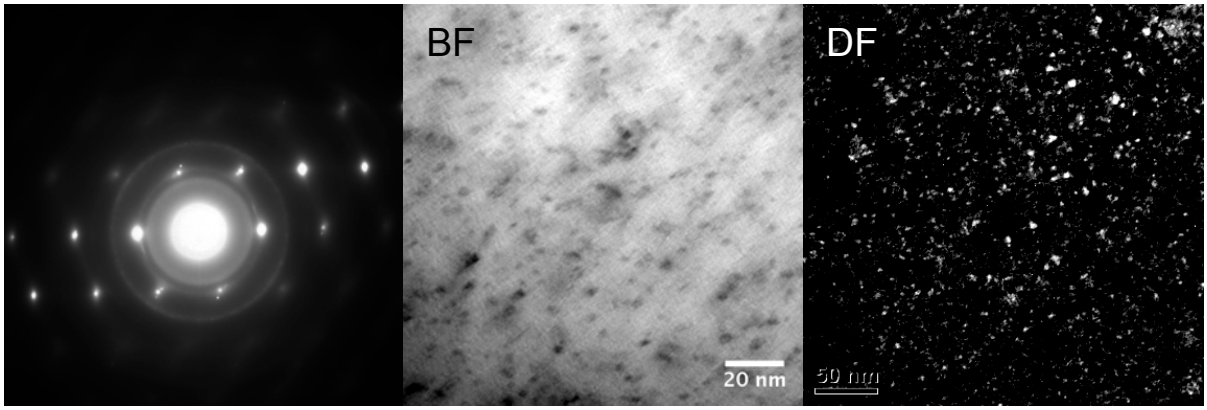

Fig. 9. Ultrafine particles and their diffraction ring pattern.

4. DISCUSSION

4.1. FRANK LOOPS

The Frank loop size distribution as a function of loop size in the KS13 compared to the previously characterized AS13, AS18, and LS13 is plotted in Fig. 10 using 1 nm bin size. Despite the similar radiation damage between the KS13 and LS13, the Frank loop distribution in the KS13 was similar to that in the AS18, but the LS13 similar to the AS13.

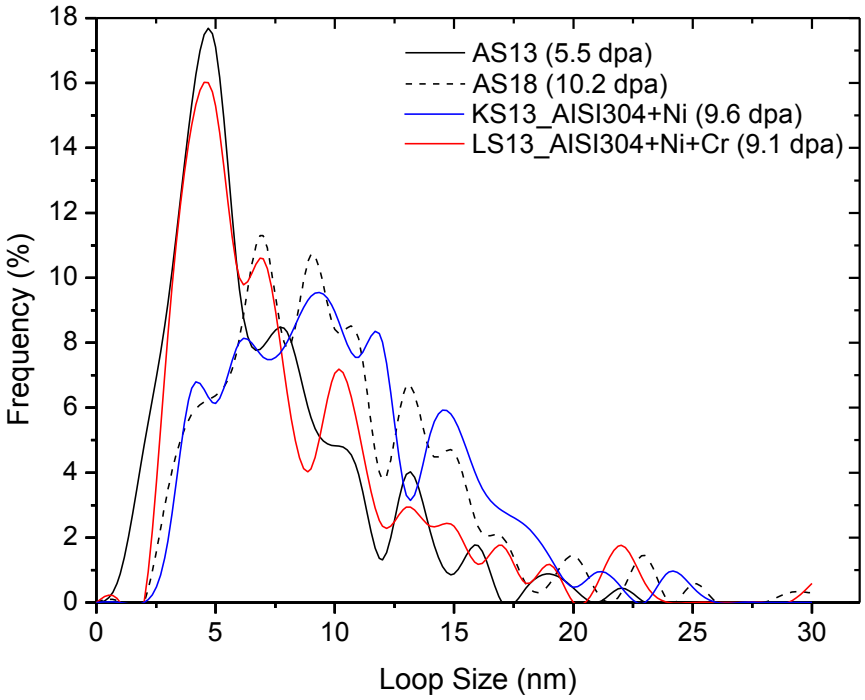

Fig. 10. Statistical result (1 nm bin size) of the Frank loops in the samples AS13, AS18, KS13, and LS13.

Comparing to the literature data as shown in Fig. 11, the average Frank loop size and density of the studied samples are consistent with the literature reports on similar materials irradiated at similar conditions. The (Ni+Cr) addition in the LS13 resulted in an intermediate size and density of Frank loops between the AS13 and AS18. In contrast, the only Ni addition in the KS13 notably reduced the loop density with some increase in loop size. This result may suggest that the Ni addition favored the coarsening and/or unfaulting of Frank loops. However, the addition of Ni together with Cr mitigated this phenomenon. The Ni-content increase resulted Frank loop density decrease is consistent with the Fe-(16-18)Cr-xNi alloys irradiated at 400°C to 0.5 dpa using protons [12]. In contrast, higher Ni-content was observed to stabilize Frank loops in Fe-15Cr-35Ni compared to Fe-15Cr-15Ni that were irradiated at 675°C and up to 84 dpa using Ni+He dual-ion experiment [13,14]. The irradiation temperature and the different dose rate between the ion and neutron irradiations may have played significant roles on the contrary effect of Ni-content on Frank loops in this class of austenitic alloys.

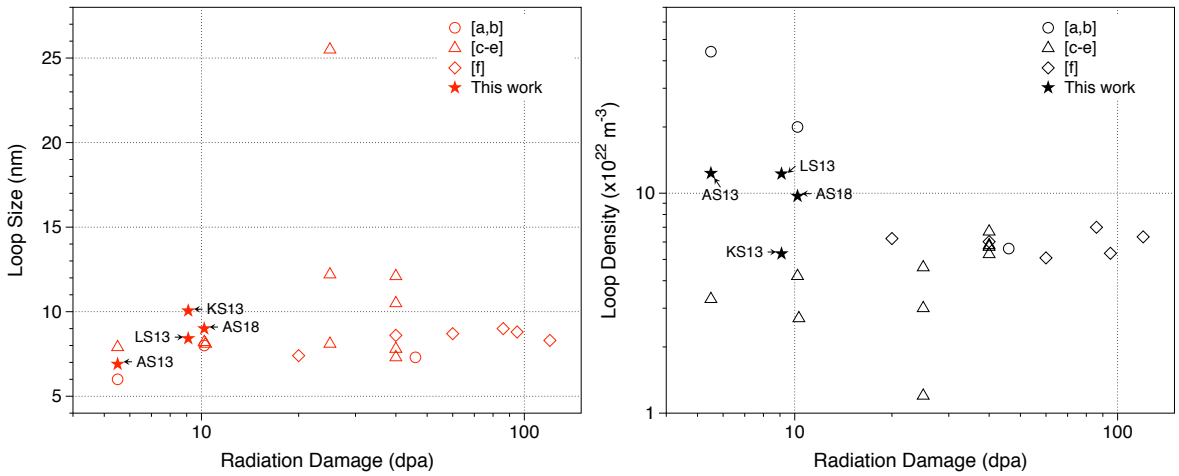

Fig. 11. Frank loop size and density as a function of radiation damage of the studied samples compared to similar materials irradiated at similar conditions [a-f corresponding to 6-11].

4.2. PHASES

The calculated results in Fig. 12 suggest that the Alloy K (+Ni) annealed at 950°C would not contain $M_{23}C_6$ in the KS13 sample. In contrast, the Alloy L (+Ni+Cr) annealed at 900°C would contain some $M_{23}C_6$ in the LS13 sample. Both samples are expected to contain a trace amount of (Ti,Cr)N. However, the volume fraction may fall below the resolution limit of TEM. $M_{23}C_6$ was observed in KS13, as shown in Fig. 6. But, its amount was much less than that in the LS13. This result is approximately consistent with the thermodynamic predictions. The $M_{23}C_6$ retained crystalline under the irradiation in both samples.

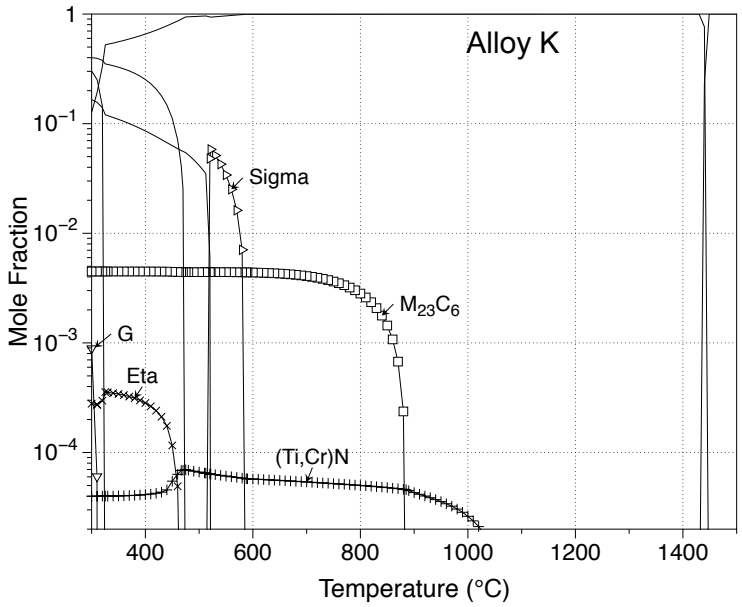

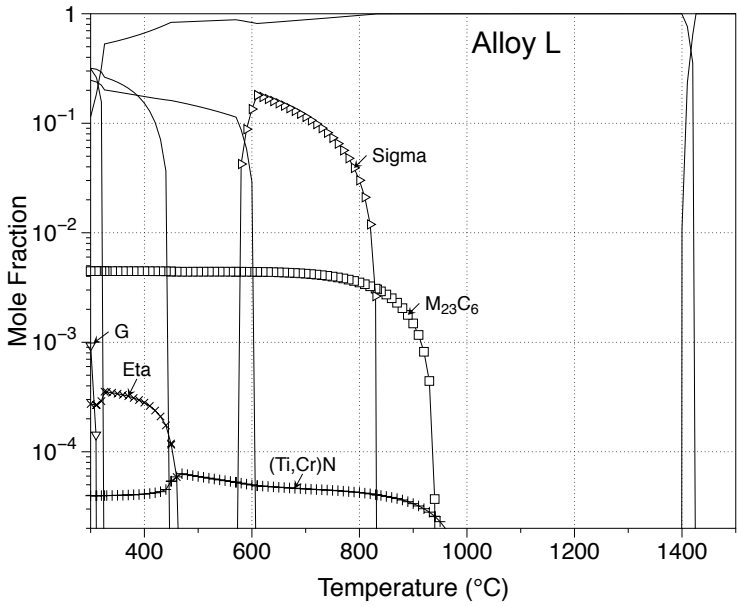

Fig. 12. Calculated temperature dependent equilibrium phase fraction in alloys K and L.

Cubic-on-cubic precipitation as shown in Figs. 2 and 4 were observed in both the KS13 and LS13. The diffraction in Fig. 2 can be a result from either $M_{23}C_6$ (Cr-rich) or G-phase (Ni/Si-rich) because they share the same crystal structure with similar lattice parameters. Chemical analysis of the ultrafine particles using EDS did not provide confident results to differentiate the two phases. However, nanoscale $M_{23}C_6$ do exist in the LS13 as shown in Fig. 13, which was not observed in the KS13.

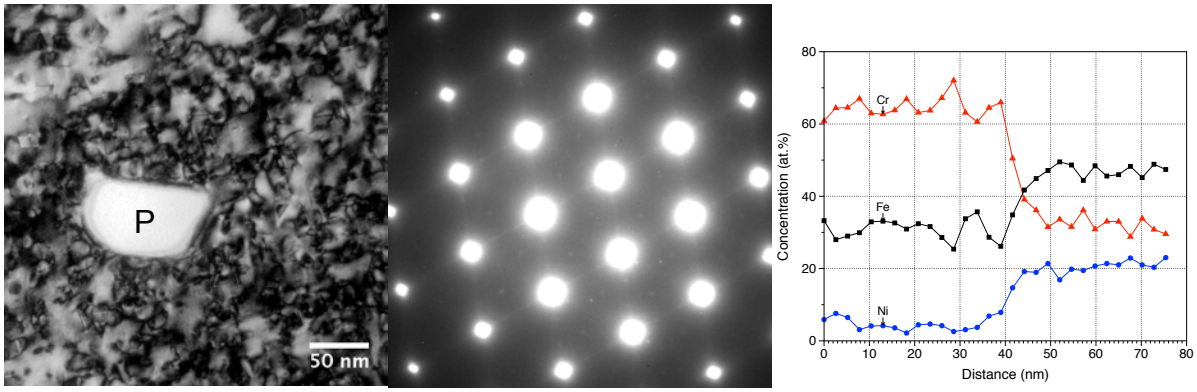

Fig. 13. $M_{23}C_6$ nano-particle (P) in the LS13 sample.

The diffraction ring pattern, as shown in Figs. 5 (KS13) and 9 (PS15), was also observed in the LS13, AS13, and AS18 samples, although the patterns in these samples were not as sharp as those in the KS13 and PS15. Additionally, such ring pattern in very dim intensity could tell in the non-irradiated alloy L sample. The stronger intensity of the ring pattern suggests that the irradiation promoted the

formation of this phase, assuming the phase is uniformly distributed in matrix. The ring patterns may have been originated from (Ti,Cr)N in the KS13, LS13, AS13, and AS18 as suggested by the preliminary indexing result of the ring pattern (Fig. 5) as well as the thermodynamic predictions of the alloys (Fig. 12). Accordingly, the ring pattern in the PS15 could be originated from HfC. Further investigation is needed to confirm the phases that resulted in the ring pattern.

In addition to the possible HfC, Laves phase, $(Fe,Ni)_2(Hf,Mo)$, was identified in the PS15. They discretely distributed at boundaries and in matrix. Their large size, in sub-micro to micrometer, may be detrimental to stress-corrosion cracking resistance of the material.

4.3. VOIDS

Radiation-induced voids were rarely observed in the KS13, as shown in Fig. 6. According to the local density of the voids about 3.2×10^{21} m^{-3}, the swelling induced by the voids would be estimated to be 0.0025%, slightly less than the estimated swelling in the AS13 and AS18. This estimation approximately follows the density measurements of the samples. Density measurement suggested much larger swelling of the LS13 compared to the other samples. However, voids were not observed in the LS13 during the previous characterization. This sample may need to be revisited.

5. CONCLUSIONS

The KS13 sample (AISI304 + Ni) has been characterized, together with a preliminary characterization of the PS15 (AISI304 + Mo + Hf). The results are compared to the previous results of the AS13, AS18, and LS13.

The Ni addition in the KS13 favored the coarsening or unfaulting of Frank loops leading to reduced density and increased size. In contrast, the Ni and Cr addition in the LS13 did not significantly alter the evolution of Frank loops. Voids were observed in the KS13, which would generate slightly smaller swelling compared to the AS13 and AS18. This is approximately consistent with density measurements of the samples.

Precipitates in the alloys were classified into two categories with one for the radiation-promoted precipitates and the other for the pre-existing ones. The pre-existing precipitates, including the large $M_{23}C_6$ (~0.2 μm) in the KS13 and LS13 and Laves phase $(Fe,Ni)_2(Hf,Mo)$ in the PS15, retained crystalline under the irradiation. The radiation-promoted precipitates include nanoscale cubic-on-cubic $M_{23}C_6$ that was observed in the LS13 but not in the KS13, cubic-on-cubic ultrafine G-phase or $M_{23}C_6$ particles (<~8 nm) with a density in the order of 10^{22} m^{-3} in both the KS13 and LS13, and a high density (10^{23} m^{-3}) of ultrafine (Ti,Cr)N (~3 nm) in all the samples (except for HfC in the PS15). The identification of the ultrafine particles was based on the diffraction patterns and thermodynamic predictions of the alloys. Further investigation, primarily chemical analyses, is needed to confirm the phases of the ultrafine particles.

6. REFERENCES

1. P. Scott, Materials Reliability Program: A Review of the Cooperative Irradiation Assisted Stress Corrosion Cracking Research Program (MRP-98), EPRI Report 1002807, 2003.
2. B. W. Arey, D. G. Atteridge, and S. M. Bruemmer, Production of Tailored Alloys to Isolate Metallurgical Variables Promoting IASCC, EPRI Report, 2007.
3. J. P. Massoud, P. Dubuisson, P. Scott, and V. K. Chamardine, CIR II Program: Description of the Boris 6 and 7 Experiments in the BOR-60 Fast Breeder Reactor, EPRI Report 1011787, 2005.
4. C. Sudha, N. Sivai Brarasi, R. Anand, H. Shaikh, R.K. Dayal, M. Vijayalakshmi, J. Nucl. Mater. 402 (2010) 186-195.
5. M. Gussev, L. Tan, J.T. Busby, Analysis of irradiation-induced phase transformations under LWR relevant conditions, Report ORNL/LTR-2012/436, Sept. 2012.
6. D.J. Edwards, A. Schemer-Kohrn, S. Bruemmer, Characterization of neutron-irradiated 300-series stainless steels, EPRI, Palo Alto, CA: 2006. 1009896.
7. D.J. Edwards, S.M. Bruemmer, Characterization of CIR II irradiated stainless steels, EPRI, Palo Alto, CA, EP-P19021/C9406, 2008.
8. Y. Yang, Y. Chen, Y. Huang, T. Allen, A. Rao, Irradiation microstructure of austenitic steels and cast steels irradiated in the BOR-60 reactor at 320°C, in: J.T. Busby, G. Ilevbare, P.L. Andresen (Eds.), 15th International Conference on Environmental Degradation, TMS (The Minerals, Metals & Materials Society), 2011.
9. Y. Chen, O.K. Chopra, W.K. Soppet, W.J. Shack, Y. Yang, T. Allen, A.S. Rao, Cracking behavior and microstructure of austenitic stainless steels and alloy 690 irradiated in BOR-60 reactor, phase I, Argonne National Laboratory, ANL/09-32.
10. Y. Yang, T.R. Allen, Y. Chen, O.K. Chopra, Dose dependence of radiation hardening of austenitic steels in Bor-60 at PWR-relevant temperatures, 14th Int. Conf. Environ. Degrad. Mater. Nucl. Power Syst., Virginia Beach, VA, US, August 23-27, 2009.
11. A.-É. Renault, C. Pokor, J. Garnier, J. Malaplate, Microstructure and grain boundary chemistry evolution in austenitic stainless steels irradiated in the BOR-60 reactor up to 120 dpa, 14th Int. Conf. on Environmental Degradation of Materials in Nuclear Power Systems, Virginia Beach, VA, August 23-27, 2009.
12. T.R. Allen, J.I. Cole, J. Gan, G.S. Was, R. Dropek, E.A. Kenik, Swelling and radiation-induced segregation in austenitic alloys, J. Nucl. Mater. 342 (2005) 90-100.
13. E.H. Lee, L.K. Mansur, Evidence of a mechanism of swelling variation with composition in irradiated Fe-Cr-Ni alloys, Philosophical Magazine A 52 (1985) 493-508.
14. W.A. Coghlan, F.A. Garner, Effect of nickel content on the minimum critical void radius in ternary austenitic alloys, in: F.A. Garner, N.H. Packan, A.S. Kumar (Eds.), Radiation-Induced Changes in Microstructure: 13th International Symposium on Effects of Radiation on Materials (1986: Seattle, Washington), ASTM International STP 955, 1987, p. 315-329.

This page intentionally left blank

INTERNAL DISTRIBUTION

1. J.T. Busby
2. K.G. Field
3. M. Gussev
4. T.M. Rosseel
5. L. Tan
6. D. Williams

EXTERNAL DISTRIBUTION

7. R. Reister, GTN Bldg, 1000 Independence Ave, S.W. Washington, DC 20585, (Richard.Reister@nuclear.energy.gov)